Numerical investigation of lift enhancement in flapping hover flight

Anand Sundaresan Bharadwaj 🆔 , and Santanu Ghosh 🆔

View Online   Export Citation   CrossMark

ARTICLES YOU MAY BE INTERESTED IN

Numerical investigation of lift enhancement in flapping hover flight

View Online   Export Citation   CrossMark

Anand Sundaresan Bharadwaj[a] [ID] and Santanu Ghosh[b] [ID]

AFFILIATIONS

Department of Aerospace Engineering, Indian Institute of Technology Madras, Chennai, Tamil Nadu, 600036, India

[a] Author to whom correspondence should be addressed: anandbharadwaj1950@yahoo.com
[b] Electronic mail: sghosh1@iitm.ac.in

ABSTRACT

The focus of this work is the study of lift enhancement in flapping hover flight using numerical simulations. An idealized set of kinematics for a NACA0012 airfoil consisting of sequential translations and rotations is considered for this purpose, such that the C_l response can be demarcated into translational and rotational parts, which facilitates comparison of forces attributed to translation and rotation. Additionally, comparisons with pure translation and pure rotation are done to isolate the effect of wing–wake interactions. The investigation reveals that the majority of lift is produced in the translational phase. The wing–wake interactions affect the translational phase of the response more than the rotational phase. However, the rotation rate determines the extent of influence of wing–wake interactions on the translational lift response. The effect of different durations of overlap between the translational and rotational motions is also assessed based on the C_l time histories and mean C_l, and the study reveals that an optimum duration of overlap can maximize the lift. An immersed-boundary method with integrated surface-load reconstruction capabilities is used for the computations presented here. The reconstruction of the surface stresses and their integration are carried out with the framework of a parallel solver. The method is validated for a flow past a NACA0012 airfoil executing a non-periodic plunge motion and a non-periodic pitch/plunge motion and a flow around an elliptic airfoil executing a flapping motion.

I. INTRODUCTION

Insects flap their wings to generate the aerodynamic forces required to keep them afloat and to perform acrobatic maneuvers. Flapping flight is known to generate high aerodynamic forces as compared to the fixed-wing flight. The reason for this is that the underlying fluid phenomena are highly unsteady.[1] The factors responsible for the production of high lift are[1] leading-edge vortex (LEV) formation (delayed stall), rotational forces, and wing–wake interactions.

Dickinson *et al.*[2] performed experiments on dynamically scaled models of insects to analyze the flow field and forces experienced in flapping flight. The effect of the timing of rotation (symmetric, delayed, and advanced) on the flow-field and the forces experienced by the wing were investigated. From the total force, a quasi-steady translational component was subtracted to reveal peaks that were attributed to rotational forces and wake capture. Two distinct peaks were reported, one of which varied with the timing of rotation

and the other did not. It was, therefore, inferred that the former peak is due to rotation and the latter is due to wing–wake interactions. It was, thereby, concluded that, to sustain high lift, the peaks due to rotation and wake capture are important mechanisms in insect flight. Early computational studies were performed by Liu and Kawachi[3] for a fluid flow past the three-dimensional hawkmoth wing in hover. It was reported that most of the lift generated was in the downstroke and latter half of the upstroke. Additionally, it was also reported that, during pronation and supination, forces generated were relatively smaller. Wang[4] reported that a two-dimensional approach to flapping can also explain lift enhancement. Wang simulated an elliptic airfoil undergoing a sinusoidal translation and rotation at a stroke plane of $\pi/3$. Positive lift, sufficient to counter the weight of a dragonfly, and thrust were predicted by the simulation. Wang *et al.*[5] later also discussed the differences in 2D and 3D flapping scenarios and reported the behavior of the leading-edge vortex in each of these cases. Sun and Tang[6] performed a computational study with kinematics similar to the one

considered by Dickinson *et al.*[2] The study reported that a peak that was attributed to the wing–wake interaction (wake capture) by Dickinson *et al.* was in fact due to the rapid acceleration of the airfoil at the beginning of the stroke. The 3D computational work of Wu and Sun[7] systematically analyzed the effect of various kinematic parameters on lift generation. The effects of varying R_e, duration of rotation, timing of rotation, and stroke amplitudes were considered. It was reported that, with increasing R_e, C_l increased and C_d dropped. Reducing the duration of rotation revealed peaks in the C_l history; however, the mean C_l was found to be quite insensitive to the duration of rotation. As far as the timing of rotation is concerned, it was reported that advancing the rotation with respect to the end of the stroke generated a higher mean C_l. They reported that the stroke amplitude greater than 90° does not affect the forces significantly. However, for values below 90°, it was reported that C_l dropped significantly with reducing stroke amplitude. Sudhakar and Vengadesan[8] performed similar studies on an airfoil flapping along an inclined stroke plane. Their work reported that the mean vertical force ($\bar{C}_v$) reduced with reducing R_e and increasing stroke amplitude, and delaying the rotation timing increased $\bar{C}_v$. The effect of varying the rotational speed on $\bar{C}_v$ was found to be negligible.

Along similar lines, many researchers have studied force generation in insect flight through wing kinematics. Bos *et al.*[9] performed computational studies to compare the overall forces produced by different kinematic models existing in the literature. Zheng *et al.*[10] combined a low-fidelity blade element model with a high-fidelity Navier–Stokes solver to understand the flight of a hawkmoth with respect to the lift forces generated and the power requirements. Sarkar *et al.*[11] investigated the effect of asymmetric flapping kinematics on forces using a discrete vortex method. Recently, Bhat *et al.*[12] studied the effect of kinematics ranging from the harmonic model to the robofly model, on the lift forces. They reported that while the overall lift history changed with translational kinematics, the magnitude of the peaks near stroke reversal was strongly influenced by the pitch kinematics. Bluman and Kang[13] studied the effect of wing–wake interactions on longitudinal stability by comparing the predictions of computational fluid dynamics (CFD) simulations that incorporated wake effects and those of quasi-steady models that neglected wake effects and thereby reported that wake effects can lead to destabilization.

Although lift production in insect flight has been studied in the past by considering quasi-steady models,[2,14] and varying kinematic parameters,[7,8] they report enhancement of lift due to a combination of the three aforementioned lift enhancement factors, and there is less clarity on how and to what extent each of these factors is individually responsible for lift enhancement. The primary aim of this work is to understand using computational simulations how each of these factors affects lift generation and to what extent they contribute to the overall lift. For this purpose, an idealized set of kinematics was adopted for a NACA0012 airfoil with sequential translations and rotations. For this set of kinematics, the airfoil never rotates and translates simultaneously at any point in the flapping cycle. In reality, the translation and rotation overlap near the end of the stroke, and this overlap may have an effect on the history of the forces experienced by the airfoil, which is also explored in this work. However, the reason for adopting kinematics without overlap is that the lift history can be demarcated into a translational part and

a rotational part, and the lift peaks can be compared. In addition, the effect of wing–wake interactions can be measured by comparing the translational and rotational parts with the corresponding pure motions (pure translation being the airfoil translating from one end of the stroke to the other starting in a quiescent medium and pure rotation being the airfoil rotating in a quiescent medium to start with). This work makes use of a direct-forcing immersed-boundary method (IBM)[15,16] for the numerical simulations of the flapping airfoil. IBMs provide an attractive option for the simulation of insect aerodynamics as these methods do not require expensive re-meshing of the grid due to the motion/deformation of the underlying (immersed) object like a flapping wing, past which the flow is simulated. Peskin, who first proposed this method,[17] has used the IBM[18] for investigation of the clap and fling mechanism in insects. Chen *et al.*[19] used the IBM to analyze the leading-edge vortex formation in the flow past an accelerating plate. Vanella *et al.*[20] used the IBM with Fluid–Structure Interaction (FSI) to study the flexibility of a hovering wing. Sudhakar and Vengadesan[8] studied the effect of kinematic parameters on the flight performance of inclined stroke plane hovering. Kumar *et al.*[21] employed the immersed-boundary method coupled lattice Boltzmann method to study the clap and fling motion. Xie and Huang[22] used immersed-boundary methods to investigate the flow field around two tandem flapping airfoils. More recently, Li *et al.*[23] used the computations from immersed-boundary methods to corroborate their experimental work investigating the flight of a dragonfly during takeoff. Zhang and Huang[24] investigated the flight of a hovering mosquito using an immersed-boundary method and reported that the advection of the trailing-edge vortex (TEV) and the production of the leading-edge vortex (LEV) were responsible for the peaks in the lift time history.

An important aspect of an aerodynamic investigation is the determination of the aerodynamic forces acting on the airfoil/wing. While this is relatively straightforward to do for CFD methods using conventional body-conformal meshes, the same is not true for IBMs, wherein the immersed surface is not generally a grid line, and as such, interpolation/extrapolation procedures are required to determine the pressure and shear stress at the airfoil surface. In this work, the methods proposed by Bharadwaj and Ghosh[16] are used, wherein estimation of surface stresses, both pressure and shear, has been performed using inverse-distance based interpolation methods. The surface-load reconstruction methods are validated for flows past a NACA 0012 airfoil executing a non-periodic plunge motion and[25] a non-periodic pitch/plunge motion[25] and an elliptic airfoil executing a flapping motion.[4]

The outline of the rest of this paper is as follows. Section II discusses the IBM used in this work. Section III presents simulations of a non-periodic plunging NACA 0012 airfoil, a non-periodic pitching/plunging NACA 0012 airfoil, and a periodically flapping elliptic airfoil. Next, Sec. IV discusses the kinematics considered and presents the results and discussions. Finally, the conclusions are presented in Sec. V.

II. METHODOLOGY

This section presents some details of the IBM used and the reconstruction methods used to determine the stress at the

immersed surface. A brief discussion is also presented on the strategy adopted to mitigate the problem of freshly cleared (FC) cells.[26] Specific details of the flow solver used are also presented.

A. Immersed-boundary method (IBM)

The IBM used in this work was initially developed for incompressible flows by Choi *et al.*[27] and subsequently extended to compressible flows by Ghosh *et al.*[28] The IBM is integrated to the REACTMB solver[29] developed at North Carolina State University.

In this method, a direct-forcing approach is used to implement the boundary conditions implicitly at the IB surface. The immersed boundary is rendered as a collection of points with the associated (local) surface-normal, and the grid cells are classified into three categories: interior cells, band cells, and field cells, based on a signed distance function (ϕ) that makes use of concepts from computational geometry. The signed distance function[27] is defined as

$$\phi(\vec{x}_k, t) = sgn\big((\vec{x}_k - \vec{x}_s) \cdot \hat{n}_s\big) \times \|\vec{x}_k - \vec{x}_s\|. \tag{1}$$

In the above equation, $\vec{x}_k$ is the position vector of the kth cell-center, $\vec{x}_s$ is the position vector of the nearest surface point, and $\hat{n}_s$ is the unit outward normal to the immersed surface at the nearest surface point. This is illustrated in Fig. 1. If $\phi < 0$, the cell is classified as an *interior* cell; if $\phi > 0$ and one of the neighboring cells is an *interior* cell, then the cell is classified as a *band* cell, or otherwise, it is classified as a *field* cell. Figure 2 illustrates the classification of the grid cells.

1. Solution forcing

The band cells are critical for the IBM since the solution forcing is performed in these cells, in order to implicitly satisfy the wall-boundary conditions. In order to apply forcing of solution in a band cell, an interpolation point and its flow properties are constructed at a position along the normal (shown in Fig. 2) to its nearest surface point.[27] Subsequently, the solution at the band cells is reconstructed.[28] Specifically, the velocity at a band cell is reconstructed as

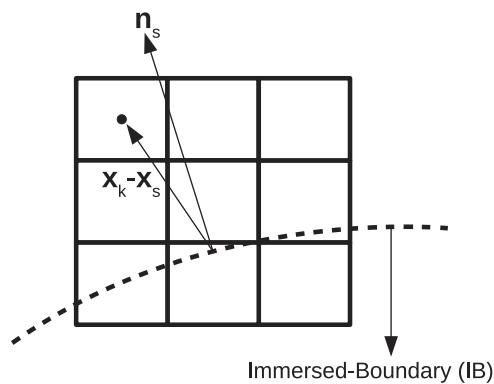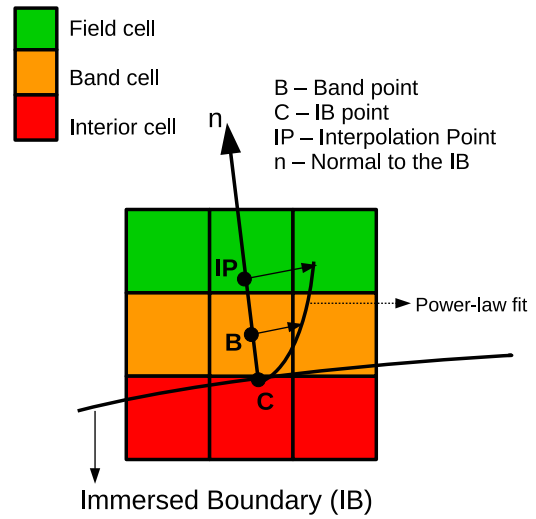**FIG. 1**. Calculation of signed distance function.

FIG. 2. Classification of cells and forcing of tangential velocity.

$$u_{B,i} - u_{w,i} = u_{T,i}(d_I)\left(\frac{d_B}{d_I}\right)^k + u_{N,i}(d_I)g(\rho, d_I, d_B),$$

$$u_{N,i}(d_I) = (u_j(d_I) - u_{w,j})n_j n_i, \tag{2}$$

$$u_{T,i}(d_I) = (u_i(d_I) - u_{w,i}) - u_{N,i}(d_I).$$

In the above equation, $u_{B,i}$ is the velocity at the band cell, $u_{w,i}$ is the velocity at the nearest wall (surface point), $u_{T,i}$ and $u_{N,i}$ are the tangential and normal velocities (relative to the surface) at the interpolation point, respectively, d_B and d_I are the distances of the band cell center and the interpolation point from the surface point, respectively, and $g(\rho, d_I, d_B)$ is a scaling function. The derivation of the scaling function is presented in Ghosh *et al.*[28] The tangential velocity in the band cell is made to follow a power law (k), which is set to unity for laminar flows and 1/7 for turbulent flows. Figure 2 shows the schematic of the reconstructed tangential velocity profile normal to the surface at the band cell obtained using a power law. Walz's relation is used to force temperature at the band cells.[28] The pressure at the band cell is extrapolated from the interpolation point, and the density is obtained by applying the equation of state using the reconstructed values of temperature and pressure.

2. Stress reconstruction at the immersed surface

Inverse-distance based interpolation methods are used to reconstruct the pressure and shear stress at the immersed surface. Specifically, pressure is reconstructed using the Inverse Distance Weight (IDW) method[16] and shear stress is determined using the interpolated gradients of velocity at the surface.[16] A 3 × 3 stencil of cell-centers built around the surface point (C) is shown in Fig. 3. The stencil is centered around cell-center B, which is the closest cell-center to the surface point. The prerequisite for a stencil to be used in the surface stress reconstruction is the presence of at least one field cell. The pressure at the surface point is then reconstructed using
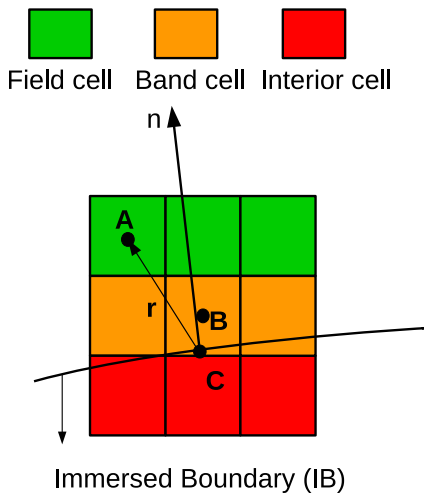
FIG. 3. Inverse Distance Weight (IDW) reconstruction.

FIG. 4. Freshly cleared cells in a moving boundary problem: "B," band cells, "I," interior cells, and "FC," freshly cleared cells.

IDW as

$$P_{IB} = P_C = \frac{\sum_i P_i/d_i}{\sum_i 1/d_i}, \tag{3}$$

where the summation holds over the field and band cells of the stencil and $d_i(=|\vec{r}|)$ is the distance between the cell-center (A) and the surface point (C).

For the reconstruction of the viscous stress, first, the velocity gradients at the field-cell centers are interpolated using the IDW method onto the surface. Subsequently, the viscous stress tensor at the surface point is constructed using the interpolated velocity gradients as

$$\bar{\bar{\tau}} = \tau_{ij} = \mu\left(\frac{\partial u_i}{\partial x_j} + \frac{\partial u_j}{\partial x_i}\right) - \frac{2}{3}\frac{\partial u_k}{\partial x_k}\delta_{ij}, \tag{4}$$

The traction vector at the surface point is then written in terms of the surface stresses as

$$\mathbf{f}_{traction} = p\hat{\mathbf{n}} + \bar{\bar{\tau}} \cdot \hat{\mathbf{n}}. \tag{5}$$

The traction vectors are subsequently integrated along the surface to estimate the loads. In the work presented here, the procedure of reconstruction and integration of surface stresses is incorporated into the parallel framework of the solver, such that the loads are calculated during the computation of the simulation. This, therefore, obviates the need to store large amounts of data to be processed offline. The surface stress reconstruction and integration in a parallel solver framework is elaborated in the Appendix.

3. Freshly cleared cells

When the immersed-body (IB) moves with respect to the grid, some cells that lie inside the solid domain, which are interior cells, emerge into the fluid domain. Such cells are known as freshly cleared
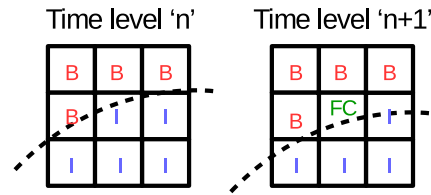
(FC) cells.[30] An issue with FC cells is that these may not contain data that are not physically correct. Figure 4 shows an interior cell (I) at the time level "n," becoming a freshly cleared (FC) cell at the time level "n + 1." An issue that arises due to the presence of non-physical data in these FC cells, which are also band cells, is that it can lead to the construction of non-physical fluxes at the interfaces of freshly cleared and field cells and consequently introduce error in the solution. To avoid this issue in this work, the FC cell is populated with a volume-weighted average of the solution of the surrounding band cells, as shown in the following equation:

$$\phi_{FCC}^{n+1,1} = \frac{\sum_i \phi_i^n V_i}{\sum_i V_i}, \text{i} \subset \text{band cell neighbors}, \tag{6}$$

where the second superscript of $\phi_{FCC}^{n+1,1}$ indicates that the volume-weighted average is populated in the FC cells at the start of the first sub-iteration of the $(n + 1)$ th time-step. It is noted that the time-step used for the simulation gets restricted by the motion of the IB, which is not allowed to move by more than a distance of one cell width during a time step. The reason for this restriction is that if the IB moves by large distances, it might end up generating freshly cleared cells from deeper within the solid domain, which will not have any band cell neighbors. Therefore, a volume-weighted average [as in Eq. (6)] cannot be performed, and consequently, the solution would become erroneous.

B. Solver details

An in-house, parallel, finite-volume solver REACTMB[31] has been used for the simulations presented in this work. The solver integrates the unsteady discretized Navier–Stokes equations in time using the Crank–Nicolson scheme, which is implicit and second-order accurate in time. Higher-order reconstruction of the state variables at the cell interfaces is done using the piecewise parabolic method.[32] Inviscid fluxes are constructed using the low-diffusion flux splitting scheme,[33] and viscous fluxes are constructed using central differences. The IBM discussed earlier in this section is integrated with the solver REACTMB.[31] To do this in the framework of an implicit time-integration method (applied for all the cells) that results in the formation of a coupled system of equations, the explicit residual vector for each cell is reconstructed as shown in the following equation, wherein the Navier–Stokes residual is combined with a source term that relaxes the primitive variable vector in the band

cells to its reconstructed value ($\mathbf{V}_{B,i}$):[31]

$$\mathbf{R}_i^{n+1,l} = (1-G)\mathbf{R}_{i,NS}^{n+1,l} + G\left[\frac{\mathbf{V}_i^{n+1,l} - \mathbf{V}_{B,i}^{n+1,l}}{\Delta t}\right]. \quad (7)$$

In the above equation, $\mathbf{R}_i^{n+1,l}$ is the residual vector, $\mathbf{R}_{i,NS}^{n+1,l}$ is the residual of the Navier–Stokes equations, l is the sub-iteration index, and G is a Heaviside function that is defined to be zero in the field cells and unity in the band (and interior) cells. Therefore, in the field cells, the solver uses the residual of Navier–Stokes equations $\mathbf{R}_{i,NS}^{n+1,l}$ to obtain the solution, and in the band cells, the solution relaxes to the forced values that are determined as discussed in Sec. II A 1. The REACTMB solver in conjunction with the IBM has been previously used to conduct parametric studies of flow-separation-control devices.[28,34,35] In this work, the solver with the integrated IBM is used to conduct simulations of flows past moving airfoils.

III. VALIDATIONS

This section presents the results of a flow past a NACA 0012 airfoil performing a non-periodic plunge motion and a NACA 0012 airfoil performing a non-periodic pitch/plunge motion and flow around a flapping elliptic airfoil. The computational details are tabulated in Table I. It is noted that the Mach (M) and Reynolds (R_e) numbers defined for the former case are based on the free-stream velocity, while for the latter, they are based on the maximum speed of translation of the elliptic airfoil.

A. NACA 0012 airfoil executing non-periodic plunge

This case involves a non-periodic plunge motion of a NACA 0012 airfoil that has its chord line parallel to the x-axis.[25] The kinematics is given by the following equation:

$$y(t) = 0.25t^2(3-t). \quad (8)$$

The simulation starts at $t = 0$ s and ends at $t = 2$ s. At $t = 2$ s, the airfoil reaches a vertical distance of 1 unit from where the motion started and comes to rest. The free-stream flow is aligned to the x-axis. A rectangular domain is used, and the domain extents are mentioned in Table I. The boundary conditions used are the velocity inlet at the left boundary and pressure outlet at the other boundaries.

TABLE I. Simulation details.

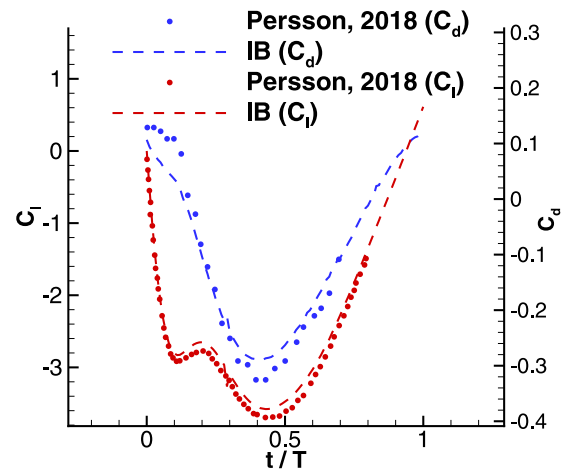|	NACA 0012 airfoil	Elliptic airfoil
M	0.2	0.3
Re_d	1000	157
Domain extents	$X \subset [-10c, 10c]$	$X \subset [-20c, 20c]$
	$Y \subset [-10c, 10c]$	$Y \subset [-10c, 10c]$
Grid size (cells)	$780 \times 1400 \times 1$	$600 \times 712 \times 1$
Grid resolution (δ_{min}) (m)	1×10^{-3}	5×10^{-3}
Time step (s)	5×10^{-4}	5×10^{-6}
Amplitude (A)	...	2.5 m
Chord/diameter (c/D)	1 m	1 m
Frequency (f)	...	40 Hz

FIG. 5. NACA 0012 airfoil in non-periodic plunge: comparison with data in the literature.

Figure 5 shows the C_l and C_d time histories obtained from the IBM closely matching with data from the literature.[25] The grid and the time-step used for the IB simulation are derived from the grid and time-step convergence studies, respectively.

B. NACA 0012 airfoil executing non-periodic pitch and plunge

This case involves a non-periodic pitch and plunge motion of a NACA 0012 airfoil.[25] The kinematics is given by the following equations:

$$y(t) = 0.25t^2(3-t), \quad (9)$$

$$\theta(t) = \frac{\pi}{3}t^2(t^2 - 4t + 4), \quad (10)$$

where y is the y-coordinate of the pivot point that is at a distance of one-third chord from the leading edge and θ is the pitch angle of the airfoil. The simulation starts at $t = 0$ s and ends at $t = 2$ s. The free-stream flow is aligned to the x-axis. A rectangular domain is used, and the domain extents are mentioned in Table I. The boundary conditions used are the velocity inlet at the left boundary and pressure outlet at the other boundaries.

Figure 6 shows the C_l and C_d time histories obtained from the IBM closely matching with data from the literature.[25] The grid and the time-step used for the IB simulation are derived from the grid and time-step convergence studies, respectively.

C. Flapping elliptic airfoil

The flow around a flapping elliptic airfoil presented here is taken from the work of Wang,[4] and the details of the flow setup are tabulated in Table I. The kinematics of the airfoil is given by

$$A(t) = \frac{A_o}{2}[\cos(2\pi t/T) + 1], \quad (11)$$

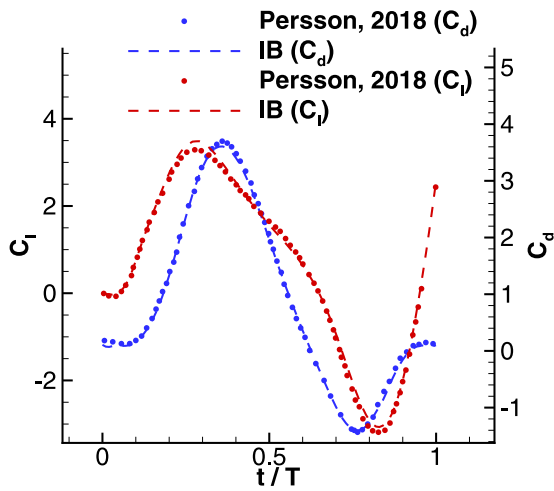$$\alpha(t) = \frac{\pi}{4}[1 - \sin(2\pi t/T)], \quad (12)$$

FIG. 6. NACA 0012 airfoil in non-periodic pitch–plunge: comparison with data in the literature.

where $A(t)$ is the position along the stroke plane inclined at $60°$ with the horizontal and $\alpha(t)$ is the angle of attack. An illustration of the flapping motion is presented in Fig. 7. The Mach number (M) and Reynolds number (Re) are based on the maximum translational velocity ($=\pi A_o f$). The Mach number is restricted to 0.3, such that the flow remains in the incompressible flow regime. The frequency of flapping is 40 Hz. As in the previous case, a rectangular domain is used, the extents of which are tabulated in Table I. The far-field boundary condition is used at all the boundaries.

Figures 8(a) and 8(b) compare C_l and C_d predicted by the IB simulation with the data in the literature[4] wherein the vertically upward direction is taken as the direction of positive lift and the
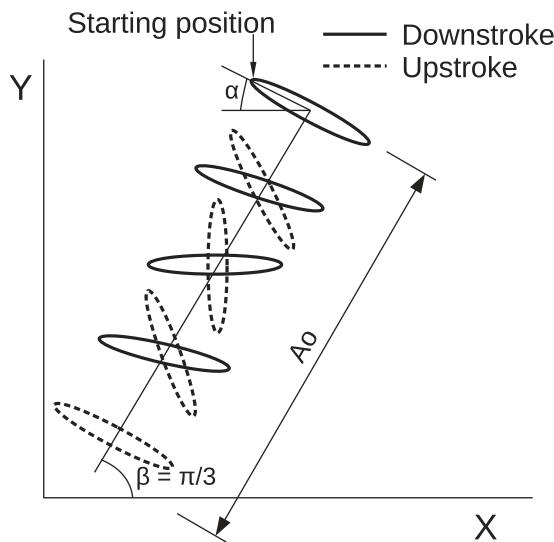

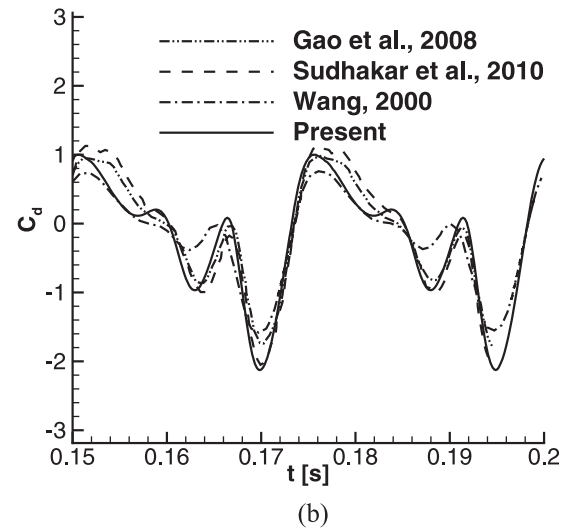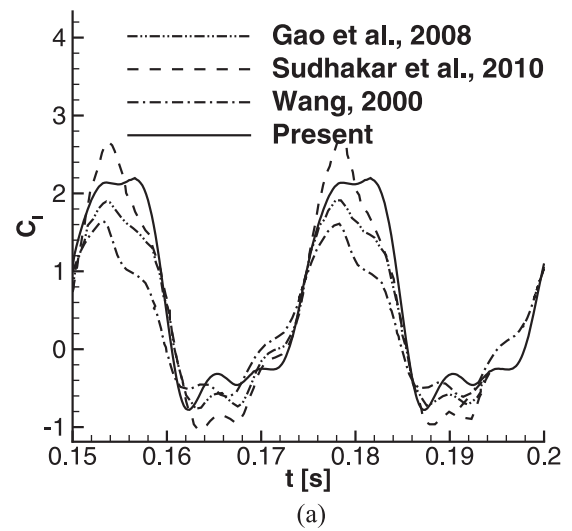**FIG. 7**. Elliptic airfoil in a flapping motion: schematic showing kinematics.

(a)

(b)

FIG. 8. Elliptic airfoil in a flapping motion: force coefficients compared with data in the literature; (a) C_l comparison; (b) C_d comparison.

rightward direction is taken as the direction of positive drag. The grid and the time-step used for the IB simulation are derived from the grid and time-step convergence studies, respectively. It is seen that C_l and C_d time histories are within the range observed in the literature.[4,8,36] It is seen that, for most of the flapping cycle, $C_l > 0$ and $C_d < 0$. This implies that the flapping mechanism produces not only lift but also thrust.

IV. LIFT ENHANCEMENT STUDY IN FLAPPING FLIGHT

In this section, the problem of flapping hover flight is considered. The methods developed for the reconstruction and integration of surface stresses are applied to this problem. In the idealized kinematics chosen, at no point in the flapping cycle does the airfoil translate and rotate simultaneously. The reason for adopting this

approach is that it will help in demarcation of the C_l response into a translation part and a rotation part and thus facilitate comparison of the lift values attributed to each phase. In addition, comparison of cases of pure translation and pure rotation (without the presence of shed vortices of previous strokes) is performed with that of the periodic motion in order to assess the influence of the wing–wake interactions on the C_l time history. Finally, cases with overlap between translational and rotational motions are considered, to assess the influence on the C_l time history and mean C_l.

The outline of this section is as follows: the kinematics and computational details associated with the simulations are discussed first; this is followed by the presentation of results for the case of pure translation and pure rotation and the three cases of flapping; finally, the results for flapping cases with overlap in translation and rotation are presented.

A. Kinematics and computational details

Figure 9 presents the schematic of an airfoil (represented by its chord) flapping according to the kinematics considered herein. The airfoil translates from point A to point B in the upstroke, with the orientation shown by the red solid line. The pitch angle ($\alpha = 45°$) remains constant until the airfoil reaches point B. After reaching point B, the airfoil rotates clockwise to orient itself along the dotted red line (at a pitch angle of $\pi - \alpha$). After the rotation is complete, the airfoil starts to translate once again during the downstroke, toward point A, at a constant pitch angle. After reaching point A, the airfoil rotates counter-clockwise in preparation for the subsequent upstroke. Figure 10 shows the variation of non-dimensional translational and angular velocities in the flapping cycle. Here, t_t is the duration of translation and t_r is the duration of rotation at the end of the stroke.

Equations (13) and (14) show the kinematics in terms of the translation and rotational velocities, respectively. These equations represent the motion for first half of the first flapping cycle. For the second half, the equations are simply multiplied with negative unity. In the following equations, t represents the time with respect to the start of the half cycle, t_1 represents the time duration for ramp up and ramp down of velocity near the end of the stroke, t_t is the duration of translation, and t_r is the duration of rotation:

$$\frac{V}{V_m} = \begin{cases} -\sin\left[\frac{\pi t}{2 t_1}\right], & t \le t_1, \\ -1, & t_1 < t \le t_t - t_1, \\ -\cos\left[\frac{\pi(t - t_t + t_1)}{2 t_1}\right], & t_t - t_1 < t \le t_t, \\ 0, & t_t < t \le t_t + t_r, \end{cases} \tag{13}$$
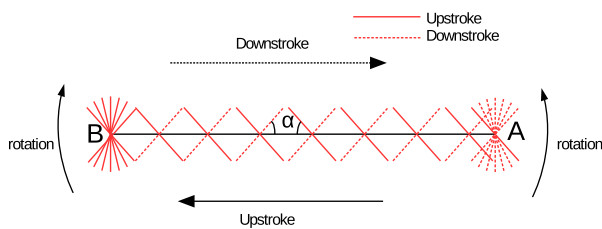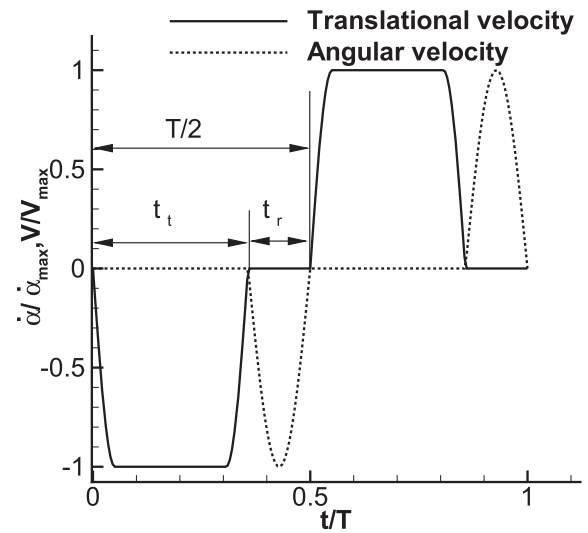
FIG. 9. Schematic of flapping kinematics.

FIG. 10. Translational and angular velocities during the flapping cycle.

$$\dot{\alpha} = \begin{cases} 0, & 0 < t \le t_t \\ \frac{-\alpha_m \pi}{t_r} \sin\left[\frac{\pi(t - t_t)}{t_r}\right], & t_t < t \le t_t + t_r. \end{cases} \tag{14}$$

The parameters cated in Table II. The Reynolds number and Mhosen for the simulations are tabulach number are calculated based on the maximum velocity of translation (V_m). All the non-dimensional coefficients such as C_l and C_p reported in this chapter are normalized with respect to the dynamic pressure based on the maximum translational velocity (V_m). The choice of R_e is the same as that in the work of Dickinson et al.[2] The direction of positive lift is taken to be the vertically upward direction. The grid size and time-step, Δt, are arrived at after performing a grid convergence study and time-step independence study, respectively. The frequencies and time durations of translation and rotation considered are tabulated in Table III. The frequencies considered are typical values encountered in insect flight.[4] The time durations are chosen such that the ratio of the duration of rotation to that of translation is around 0.4 for case 3, which is of the same order chosen previously in the literature.[6,7] The domain and the boundary conditions are shown in Fig. 11(a). The grid, shown in Fig. 11(b), is finely resolved in the region of flapping. The airfoil positions at the start and end of the upstroke and downstroke are also shown in the figure.

TABLE II. Parameters for the simulations.

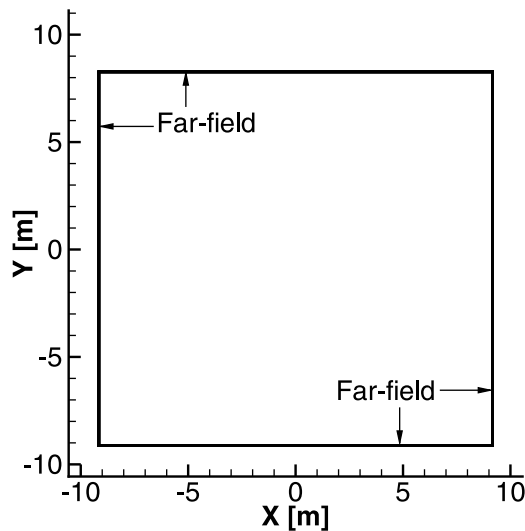|	
R_e	136
M	0.3 (based on V_m)
Length of the stroke	$2c$
Pivot	$1/4 c$
Grid size	$480 \times 280 \times 1$ cells
Grid resolution (δ_{min})	0.005 m
Δt (s)	1.0×10^{-5}
α_m	$\pi/4$

TABLE III. Time durations and frequencies for the three cases.

Case	t_t (s)	t_r (s)	f (Hz)
Case 1	0.008 92	0.014 32	21.51
Case 2	0.008 92	0.007 16	31.09
Case 3	0.008 92	0.003 58	40.0

TABLE IV. Grid convergence details.

Refinement level	Number of cells	$C_{l,mean}$
Fine	$960 \times 560 \times 1$	1.70
Medium	$480 \times 280 \times 1$	1.69
Coarse	$240 \times 140 \times 1$	1.55

B. Grid and time-step independence studies

The grid and time-step independence studies are reported for the case of pure translation of the airfoil from one end of the stroke to the other, at a constant pitch angle ($\alpha_m = \pi/4$ with respect to the

negative x-axis). The kinematics follows Eq. (13), with the simulation starting at $t = 0$ (start of translation) and ending at $t = t_t$ (end of translation).

1. Grid convergence study

For the grid independence study, three grids were considered. The grid sizes are tabulated in Table IV. From Fig. 12, it is seen that the lift time histories for the medium and fine grids are very close to each other. This is also reflected in Table IV, which reports the value of the mean C_l. It is seen that, in comparison with the coarse grid, the medium and fine grids show very close agreement. Therefore, the medium grid is used for the rest of the simulations.

2. Time-step convergence study

For the medium grid arrived at from the grid independence study, three different time-steps were used to simulate the translating airfoil. The time-steps used are $\Delta t = 1 \times 10^{-5}$ s, 5×10^{-6} s, and 1×10^{-6} s. Figure 13 shows the C_l history for the aforementioned time-steps. It is seen that the C_l histories associated with the three time-steps are virtually indistinguishable, implying time-step independence. For simulations performed henceforth, Δt is fixed to be 1×10^{-5} s.

C. Results

The variation of C_l with time for the case of pure translation is explained with the aid of C_p plots and vorticity contours at selected time instants. The C_l time history for the cases of pure rotation is
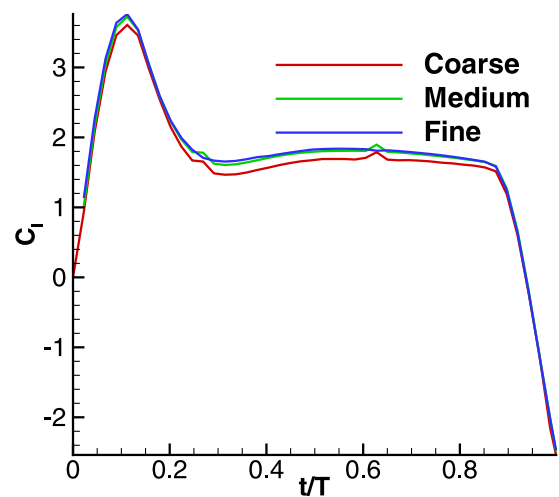

FIG. 11. Computational setup: (a) domain and boundary conditions; (b) grid: one in every ten grid lines plotted in x and y directions.

FIG. 12. Grid convergence for pure translation: T is the total time of translation.
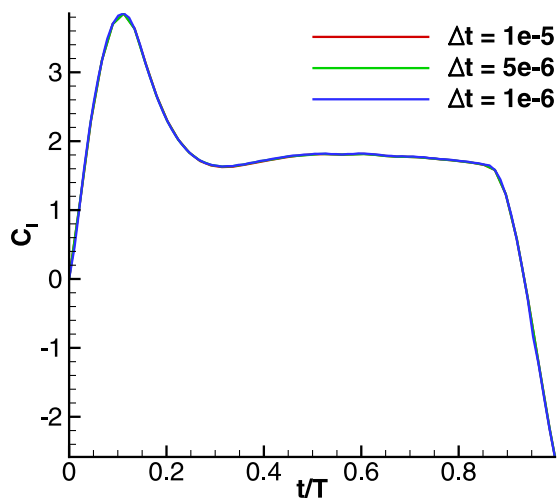
FIG. 13. Time-step convergence for pure translation: T is the total time of translation.
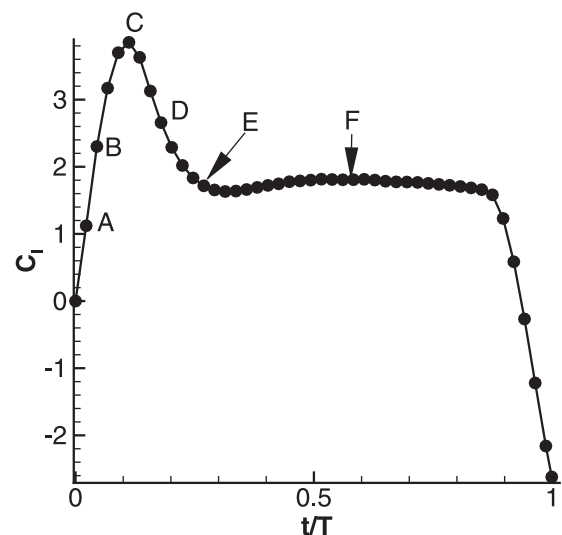

FIG. 14. C_l time history for pure translation: T is the total time of translation.

explained with the aid of vorticity contours and C_p vector plots. The time periodic response in the cases of flapping is analyzed with the aid of vorticity contours. It is noted that the vorticity contours presented in this section are normalized with the ratio of the maximum speed of translation of the airfoil (V_m) and half stroke length (unity, in this work). Additionally, the lift forces of the flapping cases are compared with those of pure translation and pure rotation to highlight the wake effects, and streamline plots are used to corroborate the findings. Finally, the C_l time histories and mean C_l for cases of varying durations of overlap between translation and rotation are compared.

1. Pure translation

For pure translation, the airfoil translates from point "A" to "B" (Fig. 9) starting in a quiescent medium, at a constant pitch angle ($\alpha_m = \pi/4$ with respect to the negative x-axis). The airfoil follows the same kinematics as mentioned in Eq. (13). The velocity of the airfoil ramps up from zero to V_m in a time duration of t_1. After attaining velocity V_m, the airfoil translates at that velocity for a duration $t_t - 2t_1$. Finally, the velocity ramps down to zero, again, in a time duration of t_1.

The C_l time history for this case is plotted in Fig. 14. It is observed that C_l reaches a peak value and then drops to a nearly constant value for the rest of the stroke. A similar qualitative trend in C_l was reported by Dickinson et al.,[2] although only the constant value attained was used to derive a quasi-steady estimate for translational lift. Here, this behavior of C_l is investigated using vorticity contours and C_p data at the surface.

Figure 15 shows the vorticity contours and the corresponding C_p data at the surface at selected time instants, as indicated by the frames "A" to "F" in Fig. 14. The C_p data plots indicate the upper surface (US) and lower surface (LS) of the airfoil. A frame by frame description is as follows.

Frame A: In frame A, the airfoil accelerates, creating a low pressure region on the upper surface (US) and a high pressure region on the lower surface (LS).

Frame B: In frame B, the airfoil continues to accelerate. The upper and lower surfaces experience lower and higher pressures as compared to those in frame A, respectively. This is seen in the C_p plots. The C_l value steadily increases as a consequence, as seen in Fig. 14. A trailing-edge vortex forms and grows in size.

Frame C: In frame C, C_l reaches a maximum value. At this time instant, the shape of the C_p plot changes as compared to the previous frames. The low pressure zone shifts to the leading edge of the airfoil. In the vorticity contours, a small region of negative vorticity appears at the trailing edge, signifying initiation of shedding of the trailing-edge vortex (TEV).

Frame D: In frame D, the airfoil has stopped accelerating and is translating at a constant velocity. The negative region vorticity at the trailing edge, associated with the shedding TEV, is more prominent in this frame. C_l assumes a lower value as compared to that in frame C, as seen in Fig. 14. Following the shedding of the TEV, the leading-edge vortex starts to develop. This is evident from the vorticity contours and the C_p plot. The blob of negative (blue) vorticity near the leading edge appears to have grown from that in frame C, which suggests the formation of the leading-edge vortex (LEV). The formation of the LEV is also suggested by the fact that the negative peak C_p at the leading edge decreases.

Frame E: In frame E, the LEV has developed to its full strength. It is seen in the C_p plot that the pressure has attained its lowest value on the upper surface. From this frame onward, the value of C_l remains nearly constant until the start of deceleration.

Frame F: In frame F, C_l is nearly the same as that in frame E. Although the C_p value at the leading edge drops, the LEV has moved along the chord, thus extending the low pressure region over a large area on the upper surface, which results in a similar lift as in frame E.

Translation, therefore, is seen to generate high values of lift. The initial surge in lift is attributed to the acceleration of the airfoil. Once the TEV is shed, the LEV starts to grow. Until the point the LEV is
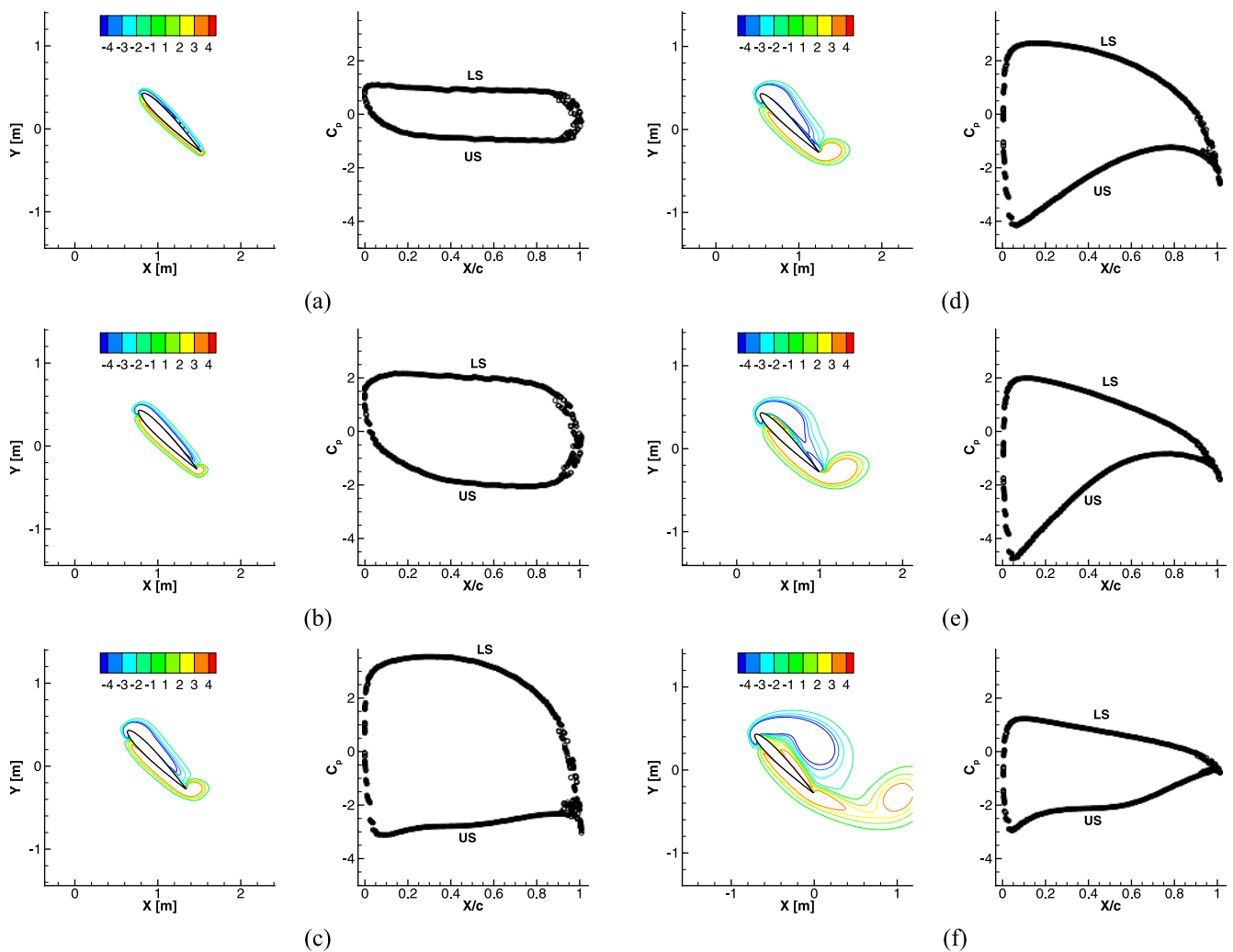
FIG. 15. Vorticity and C_p plots at different time instants: (a) frame A; (b) frame B; (c) frame C; (d) frame D; (e) frame E; (f) frame F.

fully formed, there is dip in lift, after which the LEV sustains the lift until the start of deceleration at the end of the stroke.

2. Pure rotation

In the case of pure rotation, the airfoil rotates clockwise about the quarter chord point in a quiescent medium from a pitch angle of α_m to $\pi - \alpha_m$. The C_l response for three cases of pure rotation, with the respective duration (t_r) mentioned in Table III, has been studied. Figure 16 compares the C_l time history for the three rotation durations. The case with the least duration corresponds to the highest pitch rate. It is seen that the value of maximum C_l increases with the rotation rate.

Figures 17–19 show the normalized vorticity contours and C_p vectors (vectors of magnitude C_p and direction along the inward normal), for the three cases at three different time instants during the course of rotation, $t/t_r = 0.25$, 0.5, and 0.75. The reason the

surface pressure is expressed as vectors instead of line/scatter plots is that the extent of the airfoil along the x-axis changes continuously as the airfoil rotates. The C_p vectors are shown by brown arrows, and the resultant force vector is shown by a black arrow. The resultant force vector is scaled to 3 cm/magnitude for the case with $t_r = 0.014\,32$ s and 0.5 cm/magnitude for the cases with $t_r = 0.007\,16$ s and $0.003\,58$ s, for convenient viewing.

As the airfoil starts to rotate clockwise, it creates a region of high pressure on the lower surface and low pressure on the upper surface. This is evident from the C_p vectors in Figs. 17(a), 18(a), and 19(a). The resultant force vector contributes to positive lift. As the rotation continues and the airfoil assumes a vertical orientation, the high pressure region on the left side of the airfoil and low pressure region on the right generate a nearly horizontal resultant force. Consequently, in this position, the contribution to lift is nearly zero for all three cases [Figs. 17(b), 18(b), and 19(b)]. As the
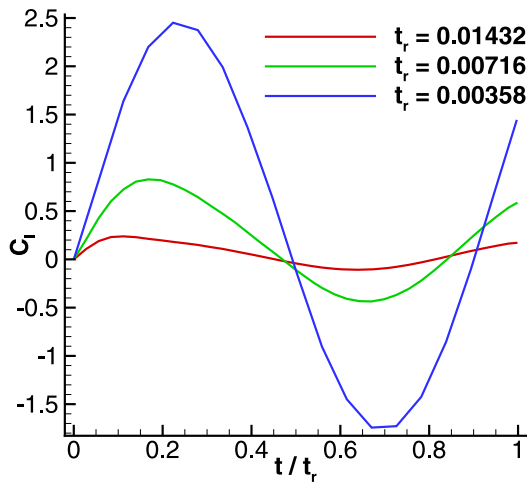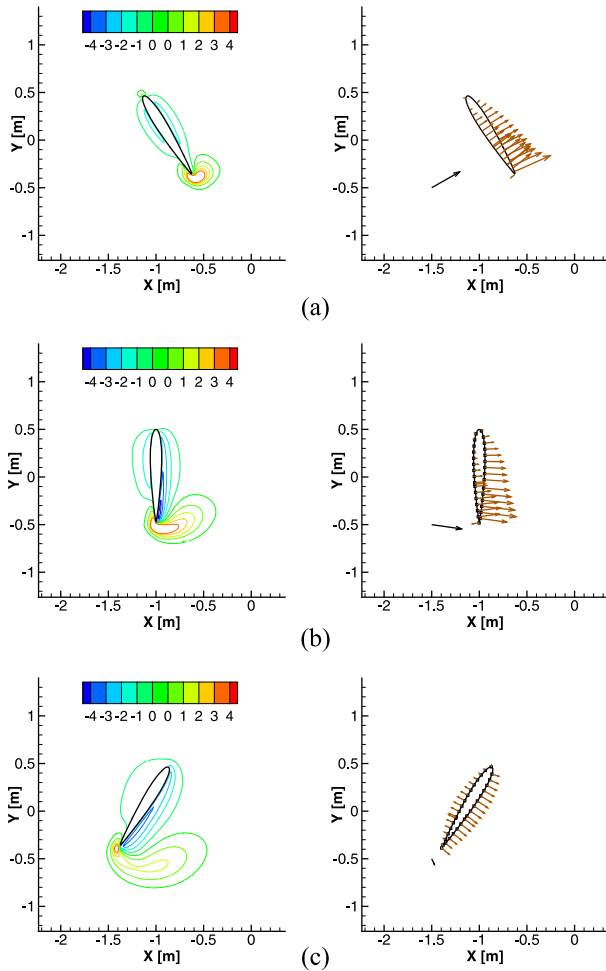
FIG. 16. C_l time history for pure rotation.

FIG. 17. Pure rotation (t_r = 0.014 32 s): vorticity contours (left column) and C_p vector plots (right column); (a) t/t_r = 0.25; (b) t/t_r = 0.50; (c) t/t_r = 0.75.
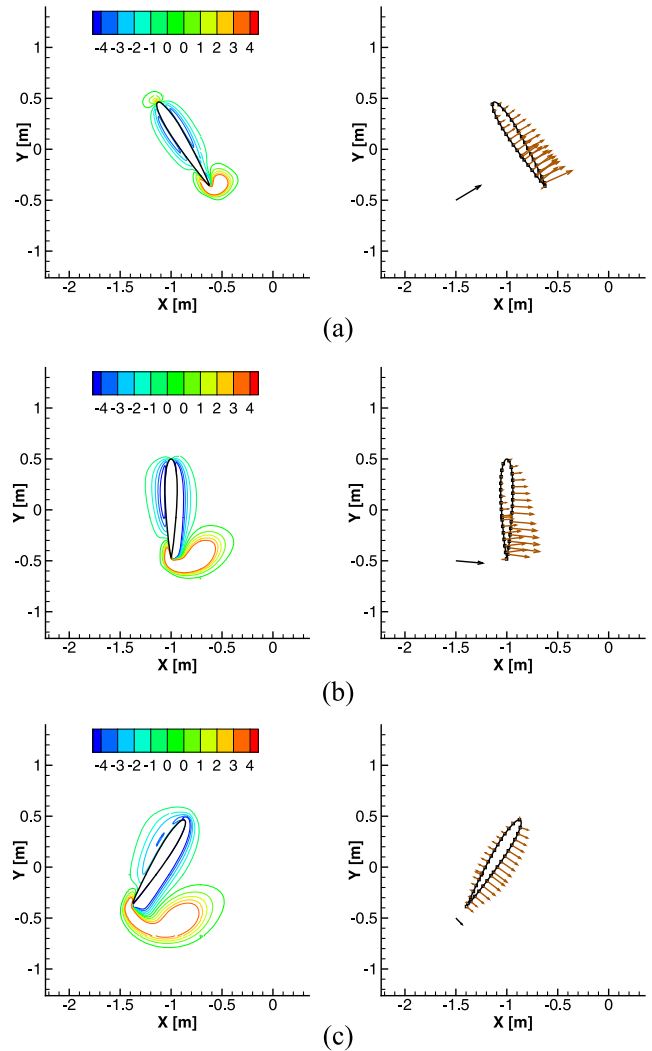

FIG. 18. Pure rotation (t_r = 0.007 16 s): vorticity contours (left column) and C_p vector plots (right column); (a) t/t_r = 0.25; (b) t/t_r = 0.50; (c) t/t_r = 0.75.

airfoil continues to rotate, the lower surface, now, has a low pressure in comparison with the upper surface, and this generates a resultant force that contributes to negative lift, as seen in Figs. 17(c), 18(c), and 19(c). This trend matches with the C_l history shown in Fig. 16. It is noted that the terms lower, upper, left, and right are used for an airfoil surface based on its position with respect to the chord line.

During the rotation, the vorticity contours appear to qualitatively obey Kelvin's circulation theorem. A region of bound vorticity is generated around the airfoil (blue contours), and a TEV of opposite polarity (red contours) is also generated. In the case with highest rotation rate, the bound vorticity and the TEV are strongest, as seen in the vorticity contours of Figs. 17–19 at corresponding time instants. The region of bound vorticity plays an important role in the lift response of the flapping case, as it tends to delay the
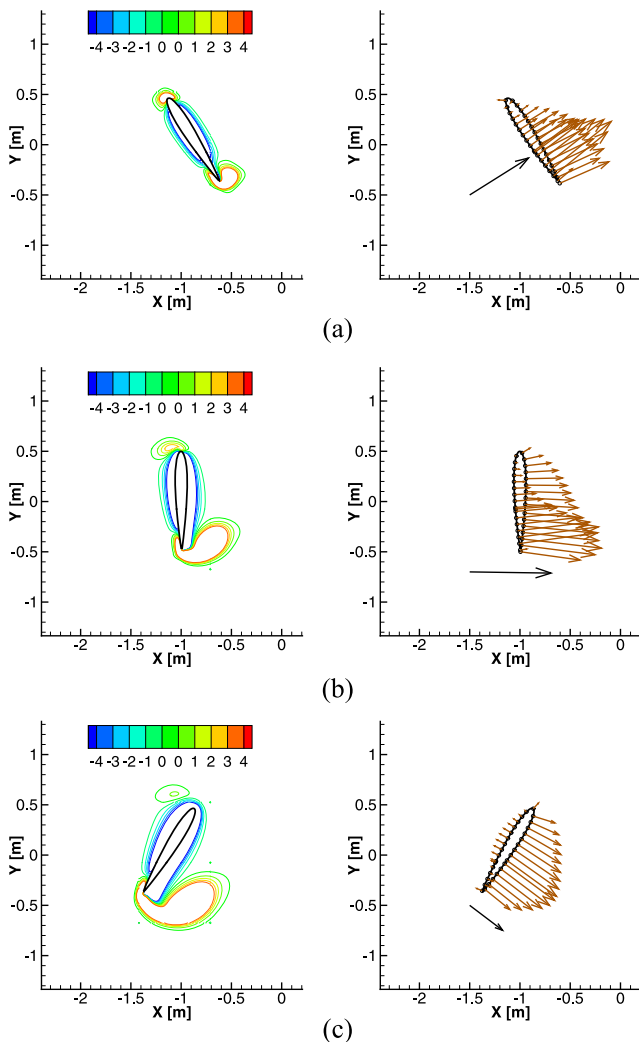
FIG. 19. Pure rotation (t_r = 0.003 58 s): vorticity contours (left column) and C_p vector plots (right column); (a) t/t_r = 0.25; (b) t/t_r = 0.50; (c) t/t_r = 0.75.

FIG. 20. C_l time histories for three different flapping frequencies: (a) case 1; (b) case 2; (c) case 3.

formation of the LEV during the subsequent translation. This is so because the LEV will assume a vorticity opposite in polarity to the bound vorticity and has to develop against the bound vorticity generated during the rotation. This will be discussed in Sec. IV C 3. It is also evident that the size of the TEV (red region of vorticity) progressively increases with the rotation rate. It is worth noting that it is these vortices that form a part of the shed wake in an airfoil executing flapping, and therefore, the wake interactions are expected to be more pronounced in cases with higher rotation rates.

3. Flapping

Figures 20(a)–20(c) show the variation of C_l for the three cases considered. In cases 1 and 2, as C_l is periodic with every cycle of flap, the vorticity contours for a single flapping cycle are shown in Figs. 21 and 22, respectively; in case 3, however, as C_l is periodic with every
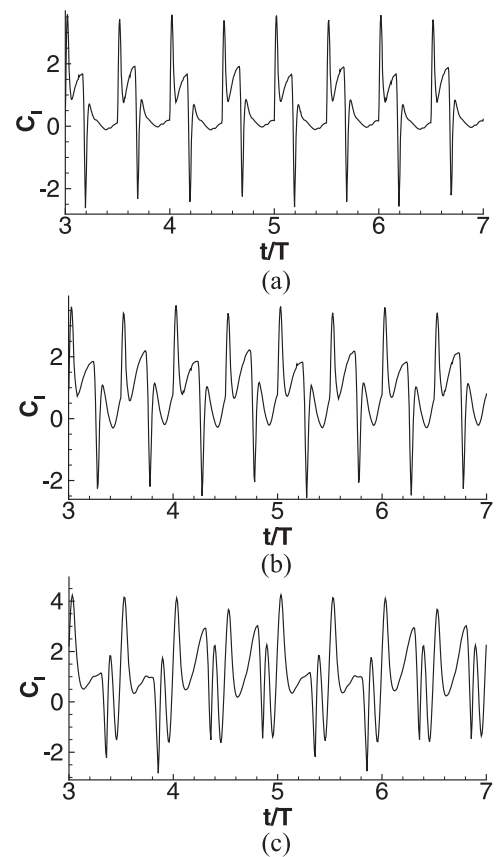
two cycles of flap, the vorticity contours for two consecutive flapping cycles (3a and 3b) are shown in Fig. 23. In these figures, the positions of the airfoil at four locations of the flapping cycle are considered. These are the positions at the beginning and end of translation in the upstroke, which are labeled P_1 and P_2, respectively, and the beginning and end of translation in the downstroke, which are labeled P_3 and P_4, respectively. The superscript in the caption denotes the flapping cycle (n). The periodicity of the flow-field is ascertained by comparing the vorticity contours at position P_1 of two consecutive cycles (n and $n + 1$) except for case 3 in which the periodicity is ascertained by comparing the vorticity contours at position P_1 of flapping cycles n and $n + 2$. The purpose of plotting the vorticity contours is to investigate the reason for different periodicity of C_l across the flapping cases simulated.

Figures 21(a)–21(d) show the vorticity contours for case 1 at positions $P_1 - P_4$. As the airfoil translates from P_1 to P_2, the LEV develops over the upper surface and a TEV is shed into the wake. In addition, the shed (blue) vortex of the previous stroke in Fig. 21(a) has advected downward with respect to the stroke plane. As the airfoil translates to P_2 in Fig. 21(b), qualitatively, the interaction between the shed vortex and the airfoil appears weak. A similar pattern is observed in the downstroke with respect to positions P_3
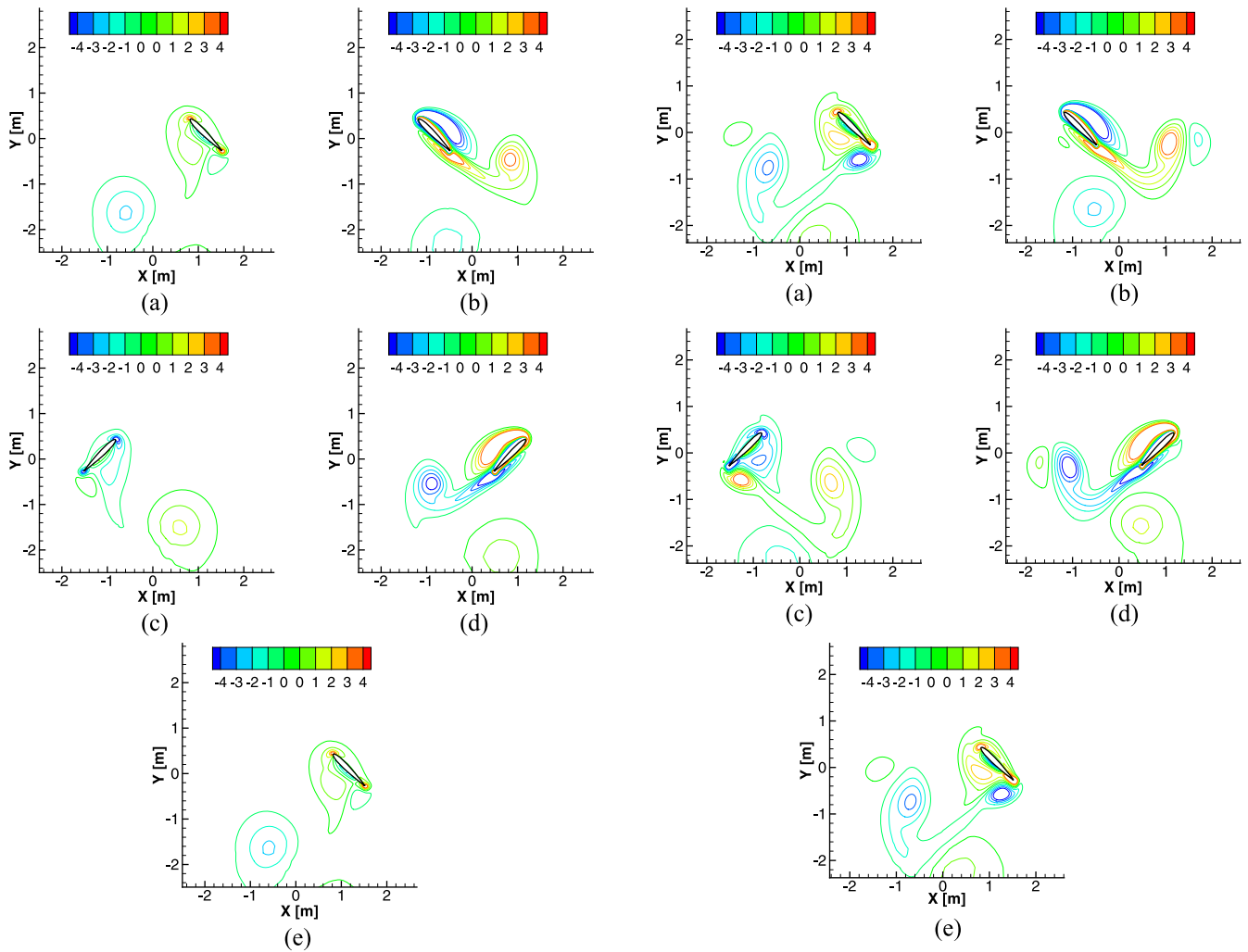
FIG. 21. Comparison of normalized vorticity contours: case 1; (a) P_1^n; (b) P_2^n; (c) P_3^n; (d) P_4^n; (e) P_1^{n+1}.

FIG. 22. Comparison of normalized vorticity contours: case 2; (a) P_1^n; (b) P_2^n; (c) P_3^n; (d) P_4^n; (e) P_1^{n+1}.

[Fig. 21(c)] and P_4 [Fig. 21(d)]. The vorticity contours at position P_1 of the subsequent cycle, P_1^{n+1}, are shown in Fig. 21(e). The plot is similar to that in Fig. 21(a), which corresponds to position P_1^n, thus reflecting the periodicity of C_l with every cycle of flap, as observed in Fig. 20(a).

Figures 22(a)–22(d) show the vorticity contours for case 2 at positions $P_1 − P_4$. As the airfoil translates from P_1 to P_2, the LEV develops over the upper surface and a TEV is shed into the wake. In addition, the shed (blue) vortex of the previous stroke in Fig. 22(a) has not advected downward, as much as in case 1. In addition, the vortex is stronger than that in case 1. As a result, the interaction between the shed vortex and the airfoil is stronger. A similar pattern is observed in the downstroke with respect to positions P_3 [Fig. 22(c)] and P_4 [Fig. 22(d)]. The vorticity contours at position P_1 of the subsequent cycle, P_1^{n+1}, are shown in Fig. 22(e). The plot is similar to that in Fig. 22(a), which corresponds to position P_1^n, as

expected. Thus, the periodic trend in the vorticity contours in case 2 is similar to that in case 1, which correlates with C_l repeating in every cycle of flap.

Figures 23(a)–23(h) show the vorticity contours for case 3 for two cycles of flap. In Fig. 23(a), the shed vortices of the previous strokes are stronger than those in cases 1 and 2. As the airfoil translates to position P_2^n, the blue colored shed vortex advects downward, as seen in Fig. 23(b). In the downstroke, shown in Figs. 23(c) and 23(d), the flow-field exhibits a similar behavior, with the red colored vortex advecting downward. At position P_1^{n+1}, the vorticity contours shown in Fig. 23(e) appear different from those corresponding to P_1^n, shown in Fig. 23(a). The orientation of the shed vortices is different at the same position of the airfoil in two consecutive flapping cycles. As the airfoil translates to position P_2^{n+1}, the blue colored shed vortex does not advect downward, as seen in the previous cycle of flap. It remains in the vicinity of the airfoil and
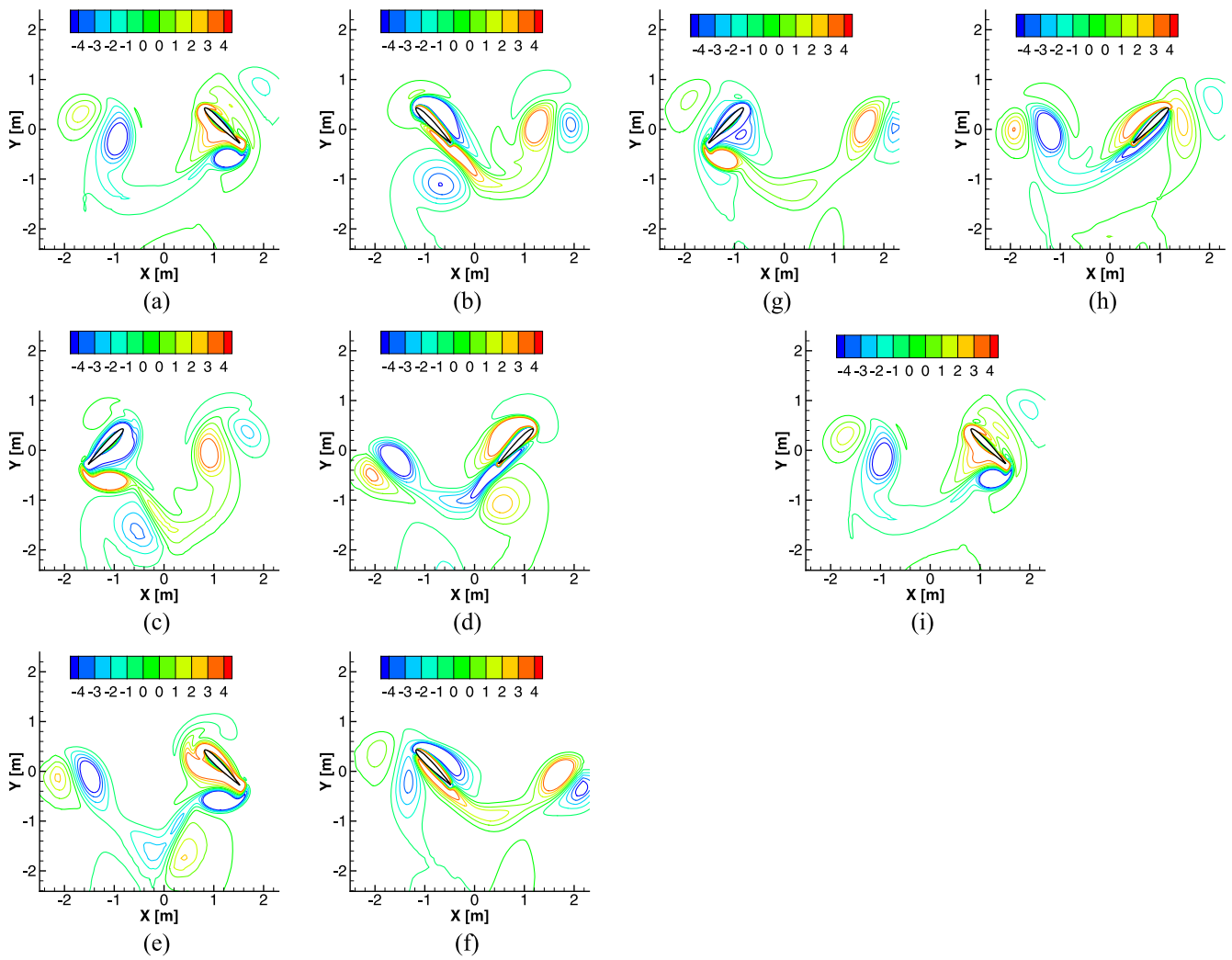
FIG. 23. Comparison of normalized vorticity contours: case 3; (a) P_1^n; (b) P_2^n; (c) P_3^n; (d) P_4^n; (e) P_1^{n+1}; (f) P_2^{n+1}; (g) P_3^{n+1}; (h) P_4^{n+1}; (i) P_1^{n+2}.

interacts with the airfoil, as the latter translates toward P_2^{n+1}. Similar observations are made in the downstroke with respect to the red colored shed vortex in Figs. 23(g) and 23(h). The vorticity contours at position P_1^{n+2} are shown in Fig. 23(i). The plot is similar to that in Fig. 23(a), which corresponds to position P_1^n, thus reflecting the periodicity of C_l with every two cycles of flap, as observed in Fig. 20(c).

The C_l contributions during translation and rotation are now investigated, along with the effect of wing–wake interactions. Figure 24 compares the C_l time history of periodic flapping with that of pure translation and pure rotation. The C_l time history of pure translation and pure rotation is overlaid on that of flapping such that the time window of pure translation matches with that of the translation part of the flapping response and likewise for pure rotation. In these figures, the time history of flapping is shown by the black solid line, and the time histories of pure translation and pure rotation

are shown by solid red and blue lines, respectively. The difference between the flapping translation response and the pure translation response is shown by the dashed red line, and the same for rotation is shown by the dashed blue line. The dashed lines thus show the effect of wing–wake interactions in each phase (translation and rotation). In Fig. 24, it is observed that, in all the cases, the translation part of the flapping response shows a higher positive C_l peak as compared to the rotation part. In case 1 and case 2, the C_l peaks during rotation are much smaller than the C_l peaks in translation due to the low rotation rates. In case 3, the peaks in rotation are higher in magnitude, but since the two peaks are nearly the same in magnitude but opposite in sense, the net lift generated during the rotation still remains small, making the translation part a more significant contributor to lift. The wing–wake interaction in the translation phase (red dotted line) appears more significant in magnitude, in comparison with that in the rotation phase (blue dotted line). The wing–wake interaction
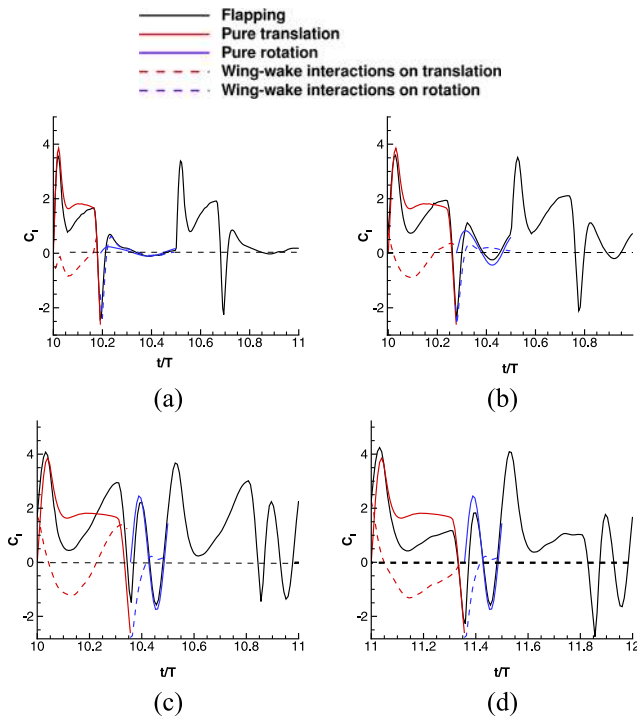
FIG. 24. Comparison of C_l time histories of flapping with those of pure translation and rotation; (a) case 1 (11th cycle); (b) case 2 (11th cycle); (c) case 3 (11th cycle); (d) case 3 (12th cycle).

TABLE V. Evaluation of wing–wake interactions: $\overline{C}_{l,t,pure} = 1.70$.

Case	$|\Delta\overline{C}_{l,w,t}|$	$|\Delta\overline{C}_{l,w,r}|$	$|\Delta\overline{C}_{l,w}|$	$\overline{C}_{l,t}$	$\Delta\overline{C}_{l,w,t}$ (%)
1	0.17	0.12	0.29	1.35	−20
2	0.25	0.18	0.43	1.48	−13
3a	0.65	0.13	0.78	1.75	3
3b	0.67	0.17	0.84	1.23	−27

in the rotation phase (blue dotted line) shows highest magnitude at the beginning of rotation and drops to low values for the rest of the rotation.

In order to evaluate the extent to which the wing–wake interactions affect the C_l time history, an average quantity is defined as

$$|\Delta\overline{C}_{l,w}| = \frac{1}{T}\int_{translation}|(C_{l,flapping} - C_{l,pure,t}|dt$$
$$+ \frac{1}{T}\int_{rotation}|(C_{l,flapping} - C_{l,pure,r}|dt. \qquad (15)$$

In the above equation, $|\Delta\overline{C}_{l,w}|$ denotes the change in magnitude of lift attributed to the wake effects averaged over a flapping cycle, $C_{l,flapping}$ denotes the instantaneous C_l of the flapping case, $C_{l,pure,t}$ denotes the instantaneous C_l of pure translation, $C_{l,pure,r}$ denotes the instantaneous C_l of pure rotation, and T denotes the time period of flapping. The first integral is computed over the two phases of translation ($2t_t$), and the second integral is computed over the two phases of rotation ($2t_r$) of the flapping cycle. The values of $|\Delta\overline{C}_{l,w}|$ for the three cases of flapping are tabulated in Table V along with the contributions from the translation part $|\Delta\overline{C}_{l,w,t}|$ and the rotation part $|\Delta\overline{C}_{l,w,r}|$, as defined by the first and second terms on the RHS of Eq. (15), respectively.

In Table V, it is seen that the overall influence (including translation and rotation) of the wing–wake interactions, $|\Delta\overline{C}_{l,w}|$, increases with the increase in the rotation rate. In all the cases, the effect

of wing–wake interactions on the translation response, $|\Delta\overline{C}_{l,w,t}|$, is higher than that on the rotational response, $|\Delta\overline{C}_{l,w,r}|$. This is also observed in Fig. 24.

It is also noted that the influence of the wing–wake interactions on the translation response, $|\Delta\overline{C}_{l,w,t}|$, increases with increasing rotation rates. This implies that as the rotation rate increases (or duration of rotation decreases) from case 1 to case 3, the vortices shed into the wake are stronger, and in addition, as the airfoil returns quickly after stroke reversal, the vortices in the wake are not allowed much time to dissipate. Therefore, the wing–wake interactions are seen to be stronger in cases with high rotation rates.

It is interesting to note that the wing–wake interactions on rotation ($|\Delta\overline{C}_{l,w,r}|$) have a narrow band of variation across the three cases of flapping. As already noted from Fig. 24, it is seen that the blue dotted line representing the wing–wake interaction in rotation is maximum at the beginning of rotation and subsequently drops to values close to zero, in all three cases. This implies that apart from the effect of the immediate wake of the preceding translation (translation being identical for all three cases), the shed wake does not significantly influence the rotational phase. This corroborates the variation of $|\Delta\overline{C}_{l,w,r}|$ within a narrow band across the three cases.

Due to the significant influence of the wing–wake interaction on the translational response, the effect on the mean lift during translation is investigated. In Table V, $\overline{C}_{l,t}$ is the mean lift during the translation phase of the flapping cycle and $\Delta\overline{C}_{l,w,t}$ is the percentage change in lift in comparison with the mean lift during pure translation, $\overline{C}_{l,t,pure}$. It is seen from the table that the wing–wake interactions appear to have an adverse effect in most cases. In cases 1 and 2, the mean lift during the translation phase of flapping is lower than that of pure translation (−20% and −13%, respectively). In case 3, however, in one cycle (3a), the wake interactions marginally enhance the lift (3%), while in the subsequent cycle (3b), their influence reduces the mean lift quite significantly (−27%).

This behavior of lift is investigated using streamline plots at the middle of the translation phase of flapping, as shown in Figs. 25 and 26. Figure 25 shows the presence of an LEV in the middle of the upstroke. It is seen that the size of the LEV reduces from case 1 to case 3, with the case of pure translation showing the largest LEV. It seems, as such, that the growth of the LEV is delayed by the presence of the bound vorticity of opposite polarity, generated by the rotation that precedes the translation. Figures 17(c), 18(c), and 19(c) show the presence of the bound vorticity at the end of rotation, shown by the blue contour lines surrounding the airfoil, generated during
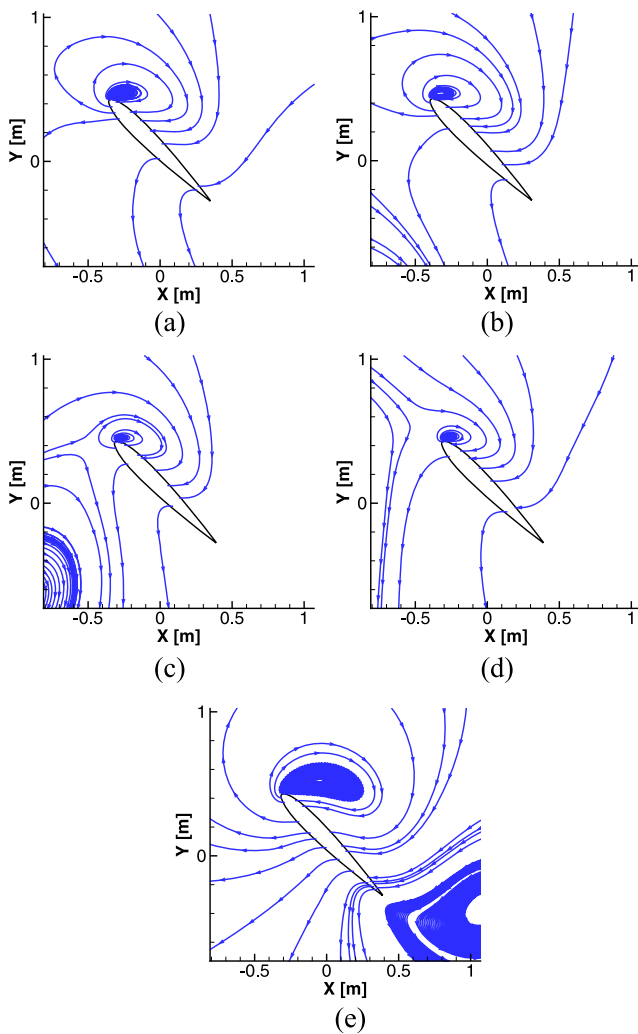
FIG. 25. Streamline patterns illustrating the size of the leading-edge vortex; (a) case 1; (b) case 2; (c) case 3a; (d) case 3b; (e) Pure translation.

FIG. 26. Streamline patterns in the presence of vortices of the shed wake; (a) case 1; (b) case 2; (c) case 3a; (d) case 3b.

rotation. High rotation rates generate high magnitude of bound vorticity. The LEV of the subsequent translation is of opposite polarity (with respect to the bound vorticity) and, therefore, has to develop against the existing bound vorticity. Therefore, a higher magnitude of bound vorticity in the case with high rotation rates causes more delay in the formation of the LEV. This is the reason for case 3 to show the smallest LEV among the three cases. It is due to this delay that all the three cases of flapping show a dip in the C_l response as compared to the case of pure translation, as seen in Fig. 24. Although the formation of the LEV is delayed, it still enhances the lift, and C_l is seen to recover after the dip (Fig. 24). However, the extent of recovery is decided by the strength and orientation of the vortices in the shed wake. In Figs. 26(a), 26(b), and 26(d), the wake vortices do not induce velocities that would aid lift generation of the translating airfoil. However, in Fig. 26(c), the wake vortices are oriented in such a way that they induce an additional free-stream velocity, thus
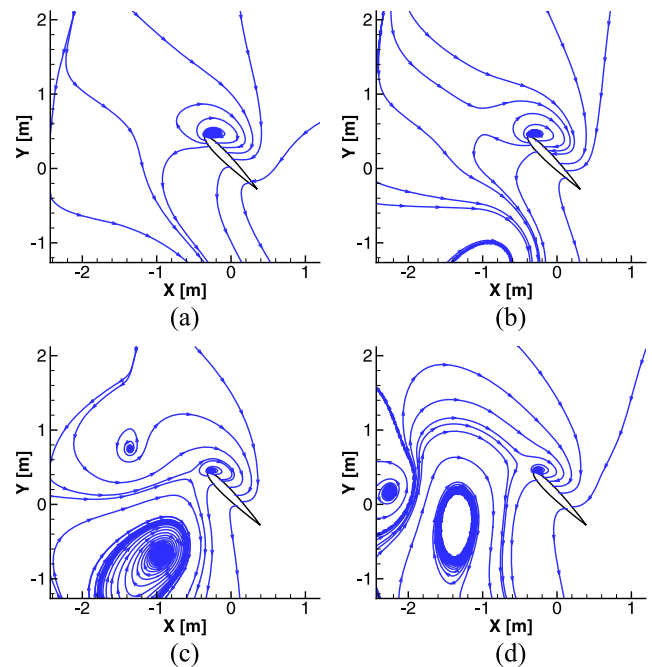
enhancing lift. This is also consistent with values of $\Delta \overline{C}_{l,w,t}$ tabulated in Table V, which reports an enhancement of lift for case 3a during translation.

4. Flapping with overlap in translation and rotation

This study investigates the effect of overlap between the translation and rotation kinematics. The reason for taking up this study is that, in general, insects translate and rotate the wing simultaneously as they flap. The duration of rotation, $t_r = 0.007\,16$, is the same as that for case 2 (Table III). Four durations of overlap, $t_{overlap}$, are considered: $t_{overlap} = 0.25t_r$, $0.5t_r$, $0.75t_r$, and t_r, in addition to case 2 presented in Sec. IV C 3, which is a case of zero overlap, i.e., $t_{overlap}$ = 0. It is noted that the rotations are symmetric about the end of the stroke; no advance and delay of rotation with respect to translation is considered. In cases with overlap unlike the study in Sec. IV C 3, the C_l time history cannot be demarcated into a translational part and a rotational part. Therefore, only the C_l peaks and mean C_l for a flapping cycle can be compared. It is noted that lift forces are produced due to a combination of translational kinematics, rotational kinematics, and wing–wake interactions and there is no apparent way to isolate these effects.

Figure 27 shows the flapping lift response for the different cases of overlap for the 10th flapping cycle, since the response in all the cases reaches a periodic state by the 10th cycle. It is seen that the maximum difference in the peaks, positive and negative, is highest in the case with zero overlap. The maximum positive peak though is observed in the case of overlap of $0.25t_r$, which marginally exceeds that of the case of zero overlap. The mean C_l, $C_{l,mean}$, for a cycle of flap for each of the cases is tabulated in Table VI. It is noted that
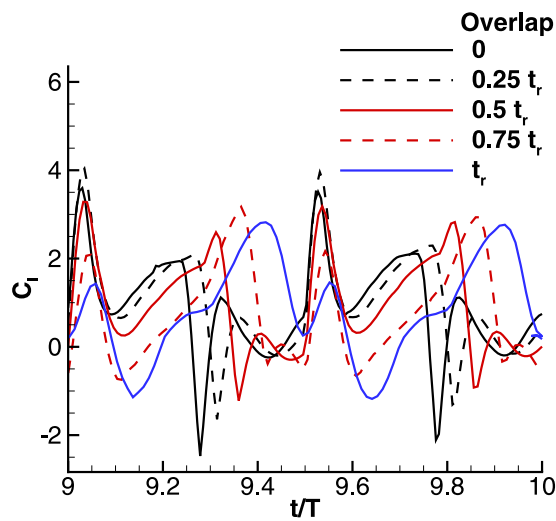
FIG. 27. Comparison of C_l time histories for five cases of overlap for the 10th cycle of flap.

TABLE VI. Comparison of mean C_l for cases with varying overlap.

Duration of overlap	$C_{l,mean}$
0	0.91
0.25 t_r	1.03
0.5 t_r	1.00
0.75 t_r	0.82
t_r	0.77

$C_{l,mean}$ increases from the case of zero overlap to the case with an overlap of $0.25t_r$, remains nearly the same for the case with an overlap of $0.5t_r$, and then drops as the overlap increases to $0.75t_r$ and t_r. Thus, a maximum mean lift likely exists for a duration of overlap between $t_{overlap} = 0$ and $0.5t_r$, indicating that an optimum overlap could enhance lift.

V. CONCLUSIONS

Investigation of the lift-enhancement mechanisms in flapping hover flight is investigated using a discrete-forcing immersed-boundary method that integrates an online post-processor for run-time interpolation and integration of surface stresses on the immersed airfoil. The airfoil kinematics primarily chosen for the problem includes distinct phases of translation and rotation with no overlap between the phases. This facilitates comparison of lift forces attributed to each phase, translation and rotation, and it is observed that, in all the three flapping cases considered, the majority of the lift is generated in the translation phase of the flapping cycle. Although the lift response in the rotational phase is not as significant as that in the translation phase, the rotation of the airfoil is still an indispensable part of the flapping cycle since it ensures that the airfoil

attains the required orientation before the following phase of translation starts. This ensures that the succeeding translation generates positive lift.

To study the effect of wing–wake interactions on lift generation, the lift response of the translational phase and rotational phase during flapping is compared with that of pure translation and pure rotation, respectively, wherein the difference in the corresponding response quantifies the effect of the wing–wake interactions. It is observed from the results that wing–wake interactions affect the translational phase of flapping more than the rotational phase. In the case of rotation, the difference between the flapping response and the pure response is highest at the beginning of rotation due to the effect of the immediate wake generated by the preceding translation. For the rest of the duration of rotation, the wing–wake interactions are much lower in magnitude. The effect of wing–wake interactions on the translational response, however, varies with rotation rates, with an increase in the magnitude of the wing–wake interaction with increased rates of rotation. This happens due to the fact that when the rotation rate is high, the vortices shed into the wake are stronger. Furthermore, due to the reduced time of rotation, the airfoil returns quickly in the subsequent stroke, without allowing much time for dissipation of the vortices in the wake that results in stronger interactions of the wake vortices with the translating airfoil. Based on the investigation presented here, it is inferred that contrary to the general notion, wing–wake interactions do not always result in lift enhancement, but their effects are dependent on the strength and the orientation of the shed vortices that in turn depend on the rotation rates.

Finally, flapping with overlap in the translational and rotational motions is also considered, and the duration of overlap is varied. It is found that the mean lift follows a trend that suggests the presence of an optimum duration of overlap for which the mean lift is maximized.

APPENDIX: SURFACE DATA AND LOAD ESTIMATION

In order to estimate the forces acting on the immersed object, inverse-distance based interpolation methods[16] have been integrated with the solver in the present work. This facilitates the calculation of surface pressure/shear stress as well as integrated loads, lift and drag, during the simulation. The load is integrated in a piecewise manner in each block and summed over the entire surface spanning across blocks, using Message Passing Interface (MPI) commands.

In a parallel framework of the solver, the immersed-boundary is present across multiple blocks of grid that are handled by separate processors. In the IBM used here, the entire immersed boundary is stored on all the processors. To illustrate, the coordinates of the circle shown in Fig. 28(a), representing the immersed-boundary,
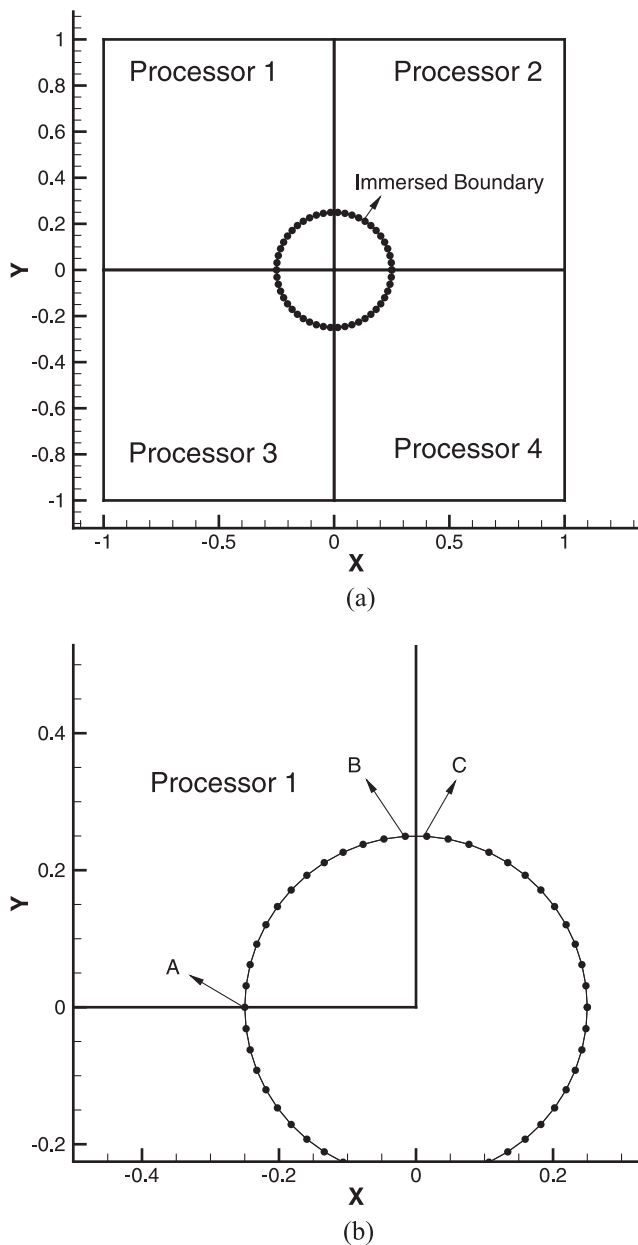
FIG. 28. Load estimation in a parallel solver framework: (a) immersed-boundary spanning across multiple blocks/processors; (b) near block boundary.

However, the process of force estimation on the panels (or line elements) requires some modification near the boundaries of the blocks, wherein a panel straddles adjacent blocks. To illustrate, in Fig. 28(b), processor 1 integrates the loads not only on panels that lie between point A and point B but also on the panel BC that spans the block/processor boundary. The reason is that when processor 2 integrates the loads on the part of the immersed-boundary lying inside its assigned block, the process would start at point C and proceed in a clockwise manner, which would imply that the element between point B and point C will not be included. However, in order to estimate the force on the panel BC, processor 1 requires the interpolated values of pressure and shear stress at point C, which are unavailable since the point is physically outside the block assigned to processor 1. Therefore, in order to estimate the forces on the panel BC, we approximate the pressure and shear stress at point C by extrapolating the values from point B.

After each processor has performed integration of the forces on the part of the immersed-boundary inside its assigned block, the values are passed to the root processor that sums all the forces and determines the total lift and drag forces and their respective coefficients.

REFERENCES

[1] S. P. Sane, "The aerodynamics of insect flight," J. Exp. Biol. **206**, 4191–4208 (2003).

[2] M. H. Dickinson, F.-O. Lehmann, and S. P. Sane, "Wing rotation and the aerodynamic basis of insect flight," Science **284**, 1954–1960 (1999).

[3] H. Liu and K. Kawachi, "A numerical study of insect flight," J. Comput. Phys. **146**, 124–156 (1998).

[4] Z. J. Wang, "Two dimensional mechanism for insect hovering," Phys. Rev. Lett. **85**, 2216 (2000).

[5] Z. J. Wang, J. M. Birch, and M. H. Dickinson, "Unsteady forces and flows in low Reynolds number hovering flight: Two-dimensional computations vs robotic wing experiments," J. Exp. Biol. **207**, 449–460 (2004).

[6] M. Sun and J. Tang, "Unsteady aerodynamic force generation by a model fruit fly wing in flapping motion," J. Exp. Biol. **205**, 55–70 (2002).

[7] J. H. Wu and M. Sun, "Unsteady aerodynamic forces of a flapping wing," J. Exp. Biol. **207**, 1137–1150 (2004).

[8] Y. Sudhakar and S. Vengadesan, "Flight force production by flapping insect wings in inclined stroke plane kinematics," Comput. Fluids **39**, 683–695 (2010).

[9] F. M. Bos, D. Lentink, B. W. Van Oudheusden, and H. Bijl, "Influence of wing kinematics on aerodynamic performance in hovering insect flight," J. Fluid Mech. **594**, 341–368 (2008).

[10] L. Zheng, T. L. Hedrick, and R. Mittal, "A multi-fidelity modelling approach for evaluation and optimization of wing stroke aerodynamics in flapping flight," J. Fluid Mech. **721**, 118–154 (2013).

[11] S. Sarkar, S. Chajjed, and A. Krishnan, "Study of asymmetric hovering in flapping flight," Eur. J. Mech.-B/Fluids **37**, 72–89 (2013).

[12] S. S. Bhat, J. Zhao, J. Sheridan, K. Hourigan, and M. C. Thompson, "Effects of flapping-motion profiles on insect-wing aerodynamics," J. Fluid Mech. **884**, A8 (2020).

[13] J. Bluman and C.-K. Kang, "Wing-wake interaction destabilizes hover equilibrium of a flapping insect-scale wing," Bioinspiration Biomimetics **12**, 046004 (2017).

[14] J. Hu, H. Xuan, Y. Yu, and J. Zhang, "Improved quasi-steady aerodynamic model with the consideration of wake capture," AIAA J. **58**, 1–8 (2020).

[15] S. Ghosh, J.-I. Choi, and J. R. Edwards, "Simulation of shock/boundary-layer interactions with bleed using immersed-boundary methods," J. Propul. Power **26**, 203–214 (2010).

[16] A. S. Bharadwaj and S. Ghosh, "Data reconstruction at surface in immersed-boundary methods," Comput. Fluids **196**, 104236 (2019).

are available on all the four processors. However, each processor, thereon, separately interpolates pressure and shear stresses only in the part of the immersed-boundary lying inside the block assigned to it. This is followed by integration of the stresses to find the forces on that part of the immersed-boundary. In order to do this, panels (or line elements) are constructed between every pair of adjacent points on the immersed boundary, and the interpolated values of the stresses (due to pressure and shear) at its end points are used for the calculation of forces using the trapezoidal rule.

[17]C. S. Peskin, "Flow patterns around heart valves: A numerical method," J. Comput. Phys. **10**, 252–271 (1972).

[18]L. A. Miller and C. S. Peskin, "Flexible clap and fling in tiny insect flight," J. Exp. Biol. **212**, 3076–3090 (2009).

[19]K. K. Chen, T. Colonius, and K. Taira, "The leading-edge vortex and quasisteady vortex shedding on an accelerating plate," Phys. Fluids **22**, 033601 (2010).

[20]M. Vanella, T. Fitzgerald, S. Preidikman, E. Balaras, and B. Balachandran, "Influence of flexibility on the aerodynamic performance of a hovering wing," J. Exp. Biol. **212**, 95–105 (2009).

[21]S. P. Kumar, A. De, and D. Das, "Investigation of flow field of clap and fling motion using immersed boundary coupled lattice Boltzmann method," J. Fluids Struct. **57**, 247–263 (2015).

[22]C.-M. Xie and W.-X. Huang, "Vortex interactions between forewing and hindwing of dragonfly in hovering flight," Theor. Appl. Mech. Lett. **5**, 24–29 (2015).

[23]Q. Li, M. Zheng, T. Pan, and G. Su, "Experimental and numerical investigation on dragonfly wing and body motion during voluntary take-off," Sci. Rep. **8**, 1011 (2018).

[24]J.-d. Zhang and W.-X. Huang, "On the role of vortical structures in aerodynamic performance of a hovering mosquito," Phys. Fluids **31**, 051906 (2019).

[25]C. F. Per-Olof Persson, in 5th International Workshop on High-Order CFD Methods, 2018, https://acdl.mit.edu/HOW5/WorkshopPresentations/CL1_HeavingAndPitchingAirfoil.

[26]J. Yang and E. Balaras, "An embedded-boundary formulation for large-eddy simulation of turbulent flows interacting with moving boundaries," J. Comput. Phys. **215**, 12–40 (2006).

[27]J.-I. Choi, R. C. Oberoi, J. R. Edwards, and J. A. Rosati, "An immersed boundary method for complex incompressible flows," J. Comput. Phys. **224**, 757–784 (2007).

[28]S. Ghosh, J.-I. Choi, and J. R. Edwards, "Numerical simulations of effects of micro vortex generators using immersed-boundary methods," AIAA J. **48**, 92–103 (2010).

[29]C. J. Roy and J. R. Edwards, "Numerical simulation of a three-dimensional flame/shock wave interaction," AIAA J. **38**, 745–754 (2000).

[30]H. S. Udaykumar, R. Mittal, P. Rampunggoon, and A. Khanna, "A sharp interface Cartesian grid method for simulating flows with complex moving boundaries," J. Comput. Phys. **174**, 345–380 (2001).

[31]S. Ghosh, "An immersed boundary method for simulating the effects of control devices used in mitigating shock boundary layer interactions," Ph.D. thesis, North Carolina State University, 2010.

[32]P. Colella and P. R. Woodward, "The piecewise parabolic method (PPM) for gas-dynamical simulations," J. Comput. Phys. **54**, 174–201 (1984).

[33]J. R. Edwards, "A low-diffusion flux-splitting scheme for Navier-Stokes calculations," Comput. Fluids **26**, 635–659 (1997).

[34]P. Sharma and S. Ghosh, "A novel vortex generator for mitigation of shock-induced separation," in *52nd Aerospace Sciences Meeting, January* (American Institute of Aeronautics and Astronautics, Reston, VA, 2014), pp. 1–16.

[35]D. Varma, S. Saurav, and S. Ghosh, "Flow control in a Mach 4.0 inlet by slotted wedge-shaped vortex generators," in *33rd AIAA Applied Aerodynamics Conference, AIAA Aviation* (American Institute of Aeronautics and Astronautics, 2015).

[36]T. Gao and X.-Y. Lu, "Insect normal hovering flight in ground effect," Phys. Fluids **20**, 087101 (2008).